

Axial and polar magnetism in hexagonal YMnO₃

S. W. Lovesey 

ISIS Facility, STFC, Didcot, Oxfordshire OX11 0QX, United Kingdom;

Diamond Light Source, Harwell Science and Innovation Campus, Didcot, Oxfordshire OX11 0DE, United Kingdom;

and Department of Physics, Oxford University, Oxford OX1 3PU, United Kingdom

 (Received 1 May 2023; revised 16 August 2023; accepted 28 August 2023; published 14 September 2023)

Newly published diffraction data on hexagonal YMnO₃ at a temperature of 10 K are shown to be consistent with a trusted expression of the magnetic symmetry, although the data alone are not definitive [M. Ramakrishnan *et al.*, *Phys. Rev. Res.* **5**, 013203 (2023)]. Howard *et al.* conclude from an exhaustive review of experimental data that the symmetry of the antiferromagnetic motif of Mn ions is most likely $P6_3'cm'$ [C. J. Howard *et al.*, *Acta Crystallogr. B* **69**, 534 (2013)]. The data reported by Ramakrishnan *et al.* do not eliminate symmetry $P6_3'$ from our calculated diffraction patterns, because the studied reflection vector is parallel to the common chiral vector associated with each triangle of Mn axial dipole moments. Proposed diffraction patterns will give decisive statements about the magnetic symmetry in future investigations using resonant x-ray and magnetic neutron diffraction. To this end, both axial magnetism and polar magnetism in the multiferroic material are essential in the analysis of diffraction patterns. We study polar magnetism in symmetry $P6_3'cm'$ using Dirac multipoles, including Mn anapoles. They also feature in amplitudes for magnetic neutron diffraction together with Dirac quadrupoles, previously shown to account for diffraction by pseudogap phases of cuprate superconductors.

DOI: [10.1103/PhysRevB.108.104412](https://doi.org/10.1103/PhysRevB.108.104412)

I. INTRODUCTION

Electronic and magnetic properties of hexagonal YMnO₃ are topics of many experimental and theoretical investigations, one reason being that it belongs to the rare class of multiferroic materials which exhibit both ferroelectricity and (noncollinear) magnetic order. The manganese trioxide is paraelectric at elevated temperatures and undergoes a single structural transition at ≈ 1250 K from a (centrosymmetric) to a (noncentrosymmetric) ferroelectric phase that is retained through room temperature [1]. The hexagonal structure hosts five- and sevenfold coordination polyhedra about Mn (Mn³⁺) and Y (Y³⁺) ions, respectively. Ferroelectricity might arise from buckling of the MnO₅ bipyramids [2]. A magnetic transition at $T_N \approx 70$ K heralds a triangular antiferromagnetic arrangement of Mn ions with a propagation vector $\mathbf{k} = 0$ [3–5]. A magneto-elastic coupling is of current interest [6,7].

By and large, structural and magnetic properties of hex-YMnO₃ have been inferred from Bragg diffraction experiments, although Fiebig *et al.* [3] demonstrate the value of second harmonic generation in determining magnetic symmetry. In $\mathbf{k} = 0$ structures, magnetic reflections arise below T_N at the same positions as the reflections of structural origin; e.g., the magnetic scattering of neutrons in general coincides with nuclear reflections. There are only a few pure magnetic reflections where structural reflections are not allowed due to the space group extinctions. The refinement of the crystal and magnetic structures using overlapping nuclear and magnetic intensities at the same reciprocal lattice positions has the problem of separating magnetic and nuclear intensities and therefore leads to correlations between the magnetic and structural parameters. Likewise with x-ray diffraction, with overlapping Thomson and magnetic intensities. Not

withstanding the mentioned limitations, there is compelling evidence that symmetry $P6_3'cm'$ correctly expresses the ordered magnetic structure of hex-YMnO₃ [5]. (Howard *et al.* critically review the existence of an intermediate phase in the transition from the paraelectric structure to the ferroelectric structure [2,5].) Another contender for the ordered magnetic structure of hex-YMnO₃ with a reduced symmetry, $P6_3'$, is also surveyed [4,5].

Bragg diffraction patterns for $P6_3'cm'$ appear not to have been published. Analytic calculations reported in this paper are informed by symmetry, and serve both neutron and x-ray diffraction. Enhancement of Bragg spot intensities obtained in resonant x-ray diffraction facilitates investigations of nominally weak Bragg spots not of structural origin, i.e., basis-forbidden reflections. We present diffraction patterns that include basis-forbidden reflections for charge-like, polar, and Dirac (polar and magnetic) atomic entities; cf. Table I. Many resonant x-ray diffraction studies using manganese *K* and *L* edges have been published [8–13]. Recent experiments on hex-YMnO₃ exploit manganese *L* edges and a relatively strong Bragg spot forbidden in the parent lattice $P6_3cm$ (No. 185) [14,15]. Howard *et al.* include symmetry $P6_3'cm'$ used here, and $P6_3c'm'$ in their group-subgroup relationships for the crystal and magnetic structures (Fig. 3), together with summaries of magnetic properties (Table I) [5]. Notably, weak ferromagnetism and a magnetoelectric effect are allowed in $P6_3c'm'$, and both these properties are forbidden by symmetry in $P6_3'cm'$.

Atomic Mn multipoles used in our diffraction amplitudes possess discrete symmetries of space and time. Polar varieties are permitted because Mn ions in hex-YMnO₃ occupy sites that do not possess a center of spatial inversion. Polar multipoles (parity odd and nonmagnetic) are allowed in diffraction

TABLE I. A generic multipole $\langle O_Q^K \rangle$ has integer rank K and $(2K + 1)$ projections Q in the interval $-K \leq Q \leq K$. Angular brackets $\langle \dots \rangle$ denote the expectation value, or time average, of the enclosed spherical tensor operator. Parity (σ_π) and time (σ_θ) signatures = ± 1 , e.g., $\langle t_Q^K \rangle$ is parity even ($\sigma_\pi = +1$) and time odd ($\sigma_\theta = -1$), and $\langle U_Q^K \rangle$ is parity odd ($\sigma_\pi = -1$) and time even ($\sigma_\theta = +1$). Special cases for neutron diffraction are a (Dirac dipole) anapole (\mathbf{d}) and Dirac quadrupole (\mathbf{H}^2) in Eqs. (C2) and (C5), respectively.

Signature	σ_π	σ_θ
Neutrons		
$\langle t_Q^K \rangle$	+1	-1
$\langle \mathbf{d} \rangle$	-1	-1
$\langle \mathbf{H}^2 \rangle$	-1	-1
Photons		
$\langle T_Q^K \rangle$	+1	$(-1)^K$
$\langle G_Q^K \rangle$	-1	-1
$\langle U_Q^K \rangle$	-1	+1

amplitudes for polar crystal structures, and they diffract x rays, and likewise for magnetic multipoles that are either parity even (conventional axial magnetism) or parity odd. Axial Mn dipoles in hex-YMnO₃ are depicted in Fig. 1 [16,17]. The polar magnetic family, Dirac multipoles, include a magnetic monopole formed with $(\mathbf{S} \cdot \mathbf{R})$, where \mathbf{S} and \mathbf{R} are electronic spin and position operators, respectively [18–20]. A generic Mn multipole $\langle O_Q^K \rangle$ has integer rank K , and angular brackets $\langle \dots \rangle$ denote an expectation value. The $(2K + 1)$ projections Q are in the interval $-K \leq Q \leq K$. Conditions on K and Q are imposed by both site and crystal symmetries, and the interaction of the radiation with electrons. Restrictions on K are imposed by the triangle rule in the case of resonant x-ray diffraction, e.g., $K = 1, 2, 3$ for enhancement by an electric dipole ($E1$)–electric quadrupole ($E2$) absorption event.

In the present case, site symmetry alone imposes the constraint that Mn axial multipoles are purely real for all K and

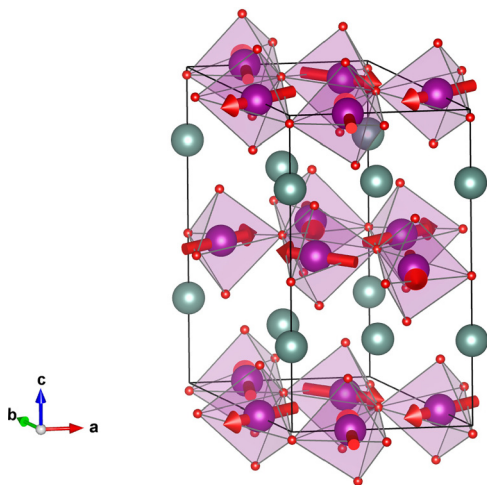


FIG. 1. Configuration of Mn axial dipoles in the (ab) plane of hex-YMnO₃. Oxygen (red) and yttrium (green) [1,5,6]. Reproduced from MAGNDATA [17].

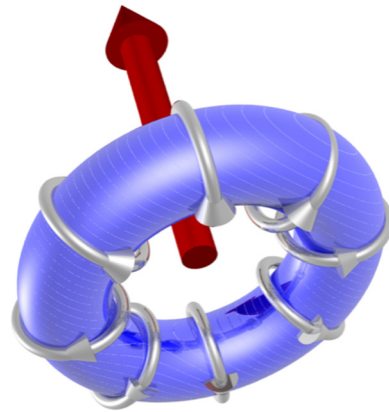


FIG. 2. Depiction of a toroidal dipole, also known as an anapole. Figure prepared by V. Scagnoli [21].

Q . From this it follows that axial dipoles are constrained to the (ac) plane, as we shall see in the next section. (Figure 1 depicts Mn dipoles without canting.) Likewise, manganese Dirac multipoles are purely real (imaginary) for even K (odd) for all Q , e.g., a magnetic monopole ($K = Q = 0$) is permitted. Projections Q are constrained by the crystal structure, however, when the reflection vector and the axis of rotation symmetry parallel to the c axis coincide. In this case, $Q = 3n$ where n is an integer. Notably, multipoles with $Q = \pm 3$ are octupoles ($K = 3$) and those of higher order. A signature of symmetry $P6_3cm'$ is a condition on a Miller index, Q , and the time signature of $\langle O_Q^K \rangle$. By way of an example of its consequences, axial magnetic dipoles are forbidden in bulk magnetism (hex-YMnO₃ is an antiferromagnet), while magnetic octupoles are permitted. An anapole depicted in Fig. 2 [18,21], perhaps the second-best known Dirac multipole beyond the magnetic monopole, also contributes to diffraction patterns. All mentioned features of hex-YMnO₃ flow from an electronic structure factor, Eq. (A1), for Mn ions in a unit cell with symmetry $P6_3cm'$. With it, diffraction patterns of x rays and neutrons can be calculated [20,22–24]. Resonant x-ray diffraction and magnetic neutron diffraction are treated in the main text and Appendix C, respectively.

II. MAGNETIC STRUCTURE

Vectors describing the hex-YMnO₃ unit cell in Fig. 1 are $\mathbf{a} = (a, 0, 0)$, $\mathbf{b} = (1/2)(-a, a\sqrt{3}, 0)$, and $\mathbf{c} = (0, 0, c)$ in an orthonormal coordinate system. Cell lengths $a \approx 6.120 \text{ \AA}$ and $c \approx 11.408 \text{ \AA}$ [6]. Local axes for Mn ions labeled (ξ, η, ζ) match orthogonal vectors \mathbf{a} , $\mathbf{b}^* \propto (\mathbf{a} + 2\mathbf{b})$, and \mathbf{c} , where \mathbf{b}^* is a vector in the reciprocal lattice.

Manganese ions occupy sites $6c$ ($\approx 0.342, 0, 0$) in space group No. 185.200 ($P6_3cm'$, BNS [16]) that possess antimirror symmetry m' along the tertiary symmetry direction $\eta = [1, 2, 0]$ [5]. A Mn multipole $\langle O_Q^K \rangle$ obeys $(\sigma_\pi \sigma_\theta 2_\eta) \langle O_Q^K \rangle = [\sigma_\pi \sigma_\theta (-1)^{K+Q}] \langle O_{-Q}^K \rangle = \langle O_Q^K \rangle$, where σ_π and σ_θ are signatures for parity and time, respectively, and are used in Table I [18,20]. In a standard setting $(-1)^Q \langle O_{-Q}^K \rangle = \langle O_Q^K \rangle^*$, where $*$ denotes complex conjugation. Whence, diagonal ($Q = 0$) multipoles are purely real. We use the phase convention $\langle O_Q^K \rangle =$

$[(O_Q^K)' + i(O_Q^K)']$ for real (single prime) and imaginary (double prime) components. Axial dipoles $\langle \mathbf{T}^1 \rangle$, say, in Table I are purely real, meaning $\langle T_\eta^1 \rangle = 0$ and $\langle \mathbf{T}^1 \rangle = (\langle T_\xi^1 \rangle, 0, \langle T_\zeta^1 \rangle)$. Looking ahead, $\langle T_\zeta^1 \rangle$ responsible for dipole canting out of the basal plane, is directly observed in resonant x-ray diffraction at basis-forbidden reflections; cf. Eq. (3).

Magnetic symmetry $P6_3'cm'$ belongs to the magnetic crystal class $6'mm'$ that is polar and compatible with the piezomagnetic effect. Ferromagnetism is not allowed. The Landau free energy includes E , EHH , and HEE , where E and H are electric and magnetic fields, respectively. The magnetic crystal class $6'$ possesses identical properties, and it is correct for symmetry $P6_3'$ in Sec. IV.

X-ray and neutron diffraction amplitudes can be derived from an electronic structure factor,

$$\Psi_Q^K = [\exp(i\boldsymbol{\kappa} \cdot \mathbf{d}) \langle O_Q^K \rangle_{\mathbf{d}}], \quad (1)$$

where the implied sum runs over the six Mn ions at sites \mathbf{d} in a unit cell. The reflection vector $\boldsymbol{\kappa} = (h, k, l)$ with integer Miller indices. Manganese sites in a cell of hex-YMnO₃ are related by threefold rotations about the c axis, and anti-sixfold rotations about the c axis with translations $\mathbf{c}/2$. Since rotations about the c axis do not change Q , the electronic structure factor is proportional to $\langle O_Q^K \rangle$ at the cell origin. A complete version of Ψ_Q^K for sites $6c$ in $P6_3'cm'$ is given in Eq. (A1).

Evaluated for a reflection vector $\boldsymbol{\kappa} = (0, 0, l)$ it reduces to

$$\Psi_Q^K(6c) = \langle O_Q^K \rangle [1 + \sigma_\theta (-1)^{l+Q}] [1 + 2 \cos(2\pi Q/3)], \quad (2)$$

which is appropriate for experiments reported by Ramakrishnan *et al.* [14]. Later, we consider $\boldsymbol{\kappa} = (h, 0, l)$. The second bracket in Eq. (2) is different from zero for $Q = 0, \pm 3$, etc. Conditions imposed on Q are the mentioned consequence of the alignment of $\boldsymbol{\kappa}$ and a triad axis of rotation symmetry in the crystal. Evidently, crystal and magnetic symmetries are interrelated in a nonzero value of the first bracket. Nuclear ($K = 0$) and Thomson multipoles are time even and $\sigma_\theta = +1$. Axial multipoles ($\sigma_\pi = +1$) in resonant x-ray diffraction have an even rank, but this restriction on K does not apply to Dirac multipoles ($\sigma_\pi = -1$).

III. RESONANT X-RAY DIFFRACTION

An atomic resonance in the x-ray absorption spectrum is often a sharp feature [13,25]. In which case, it is meaningful to assign an amplitude to the resonant contribution equal to its energy-integrated intensity. The four amplitudes are labeled by polarization states depicted in Fig. 3, and they can be developed in electronic multipoles introduced in Sec. I [19,20,26]. Analytic expressions for axial and Dirac multipoles for an informative atomic model are listed by Lovesey and Scagnoli [18]. In our notation, $(\pi'\sigma)$ denotes a rotated amplitude, and $|(\pi'\sigma)|^2$ the intensity of the Bragg spot enhanced by the atomic resonance [18,20]. Universal expressions for diffraction amplitudes employed here are functions of the rotation of the illuminated crystal about the reflection vector by an angle ψ [26].

Parity-even ($E1-E1$, $E2-E2$) Mn multipoles denoted $\langle T_Q^K \rangle$ satisfy $(-1)^Q \langle T_{-Q}^K \rangle = \langle T_Q^K \rangle$; i.e., multipoles are purely real $[\sigma_\theta (-1)^K = +1, \sigma_\pi = +1 : E1-E1, K = 0-2;$

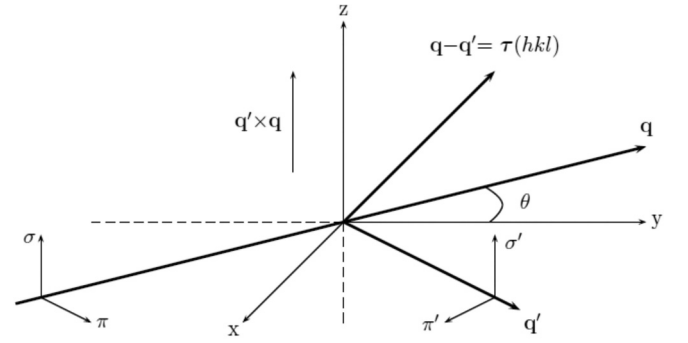


FIG. 3. Primary (σ, π) and secondary (σ', π') states of polarization. Corresponding wave vectors \mathbf{q} and \mathbf{q}' subtend an angle 2θ . The Bragg condition for diffraction is met when $\mathbf{q} - \mathbf{q}'$ coincides with a vector $\boldsymbol{\tau}(h, k, l)$ of the reciprocal lattice. Crystal vectors \mathbf{a}, \mathbf{b}^* , and \mathbf{c} , which define local axes (ξ, η, ζ) and the depicted Cartesian (x, y, z) coincide in the nominal setting of the crystal.

$E2-E2, K = 0-4$]. Dirac multipoles $\langle G_Q^K \rangle$ possess discrete symmetries $\sigma_\pi \sigma_\theta = +1$, whence $E1-E2$ multipoles are purely real (imaginary) for even K (odd K). Specifically, a magnetic charge (monopole $\langle G_0^0 \rangle$) that contributes in an $E1-M1$ event ($K = 0-2$) is allowed by site symmetry.

Returning to Eq. (2), we consider basis-forbidden reflections with odd l . Conditions for nonzero Ψ_Q^K are as follows: $E1-E1$ and $E2-E2$; odd $K + Q$; $E1-M1$ and $E1-E2$; even K and $Q = 0$ for Dirac multipoles. Diagonal ($Q = 0$) contributions to $(0, 0, l)$ x-ray diffraction amplitudes do not depend on the azimuthal angle.

Unrotated $E1-E1$ amplitudes are zero for $\boldsymbol{\kappa} = (0, 0, l)$ with odd l , i.e., $(\sigma'\sigma)_{11} = (\pi'\pi)_{11} = 0$. Whereas, $(\pi'\sigma)_{11}$ is proportional to the axial dipole moment along the crystal c axis, $\langle T_\zeta^1 \rangle$. Specifically, $(\pi'\sigma)_{11}$ is purely imaginary with [26],

$$(\pi'\sigma)_{11} = (i3\sqrt{2}) \sin(\theta) \langle T_\zeta^1 \rangle, \quad (3)$$

where θ is the Bragg angle depicted in Fig. 3. An $E2-E2$ amplitude contains a hexadecapole; see below. Equal intensities are observed in Bragg diffraction by hex-YMnO₃ at Mn L_2 and L_3 edges [14]. This result implies a null orbital contribution from $3d$ ($4p$) electrons sampled in an $E1-E1$ ($E2-E2$) absorption event. The reasoning is as follows. Reduced matrix elements (RMEs) for both parity-even events are $(A + B)$ and $(2A - B)$ for L_2 and L_3 edges, respectively (e.g., [27] and Eq. (73) in Ref. [20]). Here, A is proportional to the orbital angular momentum in the $3d$ or $4p$ states. On the other hand, B includes expectation values of spin and hybrid spin-orbital operators. RMEs for K edges are independent of spin variables ($B \equiv 0$) [28]. More information on sum rules is given in Appendix B.

Unrotated Dirac $E1-E2$ amplitudes are zero while, in keeping with $E1-E1$,

$$(\pi'\sigma)_{12} = (3/2\sqrt{5}) [1 - 3 \cos(2\theta)] \langle G_0^2 \rangle. \quad (4)$$

Note the 90° phase shift between $E1-E1$ and $E1-E2$ diffraction amplitudes. Intensities are in quadrature and interference between $E1-E1$ and $E1-E2$ intensities does not exist.

An anapole, illustrated in Fig. 2, $\langle G_\eta^1 \rangle = -\sqrt{2} \langle G_{+1}^1 \rangle'$ contributes to all $(h, 0, l)$ diffraction amplitudes, and we provide

$(\sigma'\sigma)_{12}$ by way of an example. To this end, $r = a/c$, and

$$\sin(\beta) = rl\sqrt{3}/Z, \quad \cos(\beta) = -2h/Z,$$

$$\text{with } Z = \sqrt{4h^2 + (rl\sqrt{3})^2}. \quad (5)$$

From the electronic structure factor, Eq. (A1), evaluated for $(h, 0, l)$ and odd l ,

$$\begin{aligned} (\sigma'\sigma)_{12} &= i(2/5)\sqrt{2} \sin(2\pi hx) \cos(\theta) \cos(\psi) [3\langle G_{+1}^1 \rangle'' \\ &+ \sqrt{5} \cos(2\beta) \langle G_{+1}^2 \rangle' + 5\{2 + 18\cos^2(\beta)\cos^2(\psi) \\ &- 13\cos^2(\beta) - 3\cos^2(\psi)\} \langle G_{+1}^3 \rangle'']. \end{aligned} \quad (6)$$

The amplitude $(\pi'\sigma)_{12}$ in the rotated channel of polarization has contributions proportional to $[\sin(2\beta)\langle G_{+1}^2 \rangle']$ and $[\sin(2\beta)\langle G_{+1}^3 \rangle'']$ in addition. Reflections of the type $h = 3n$ are weak for hex-YMnO₃ since the general coordinate x is close to $1/3$. When the azimuthal angle $\psi = 0$ the crystal axis \mathbf{b} and $\boldsymbol{\eta}$ coincide. The diffraction condition $(h, 0, l)$ with odd l is not satisfied at Mn L edges ($L_2 \approx 0.649$ keV and $L_3 \approx 0.638$ keV), and it is at the K edge (≈ 6.537 keV) for a range of h and l .

There is no diffraction by polar $E1-E2$ multipoles $\langle U_0^K \rangle$ for odd l . Likewise for the rotated channel of polarization and $(0, 0, l)$ with even l . Diagonal polar multipoles with odd K diffract in the unrotated channels, however. The dipole $\langle U_0^1 \rangle$ is the average displacement of the Mn ion along the crystal c axis, and for a reflection vector $(0, 0, l)$ with even l ,

$$\begin{aligned} (\sigma'\sigma)_{12} &\propto i \sin(\theta) [\sqrt{3}\langle U_0^1 \rangle - \sqrt{2}\langle U_0^3 \rangle], \\ (\pi'\pi)_{12} &\propto i [\sqrt{3} \sin(3\theta) \langle U_0^1 \rangle \\ &+ \sqrt{2} \sin(\theta) \{1 + \cos^2(\theta)\} \langle U_0^3 \rangle]. \end{aligned} \quad (7)$$

Amplitudes do not depend on the azimuthal angle, as expected.

Returning to $\kappa = (0, 0, l)$ with odd l , the $E2-E2$ amplitude $(\pi'\sigma)_{22}$ possesses a signature of the triad axis of rotation symmetry along the c axis, in that $(\pi'\sigma)_{22}$ is threefold periodic in the azimuthal angle ψ . An $E2$ absorption event at the L edges uses electronic states $2p \rightarrow 4p$, and a hexadecapole $\langle T_{+3}^4 \rangle'$ is permitted. Specifically,

$$\begin{aligned} (\pi'\sigma)_{22} &= (3/\sqrt{10}) (-i \{ \sin(3\theta) \langle T_{+3}^1 \rangle_{\xi} \\ &+ \sin(\theta) [2 - 3\cos^2(\theta)] \langle T_0^3 \rangle \} \\ &+ \sqrt{5} \cos^3(\theta) \cos(3\psi) \langle T_{+3}^4 \rangle'). \end{aligned} \quad (8)$$

The azimuthal angle scan starts with the crystal axis \mathbf{a} normal to the plane of scattering. Notably, magnetic and charge-like contributions to $(\pi'\sigma)_{22}$ differ by a 90° phase and intensities are in quadrature.

IV. REDUCED SYMMETRY

Howard *et al.* reject symmetry $P6_3'$ for hex-YMnO₃ for several reasons, and to further refine the debate about its relevance we survey the diffraction properties of $P6_3'$ (No. 173.131 BNS) [4,5]. The c -glide plane perpendicular to

$[1, 0, 0]$ (and $[0, 1, 0]$ and $[-1, -1, 0]$) and mirror plane perpendicular to $[1, -1, 0]$ (and $[1, 2, 0]$ and $[-2, -1, 0]$) are lost in $P6_3'$, and the chiral vector parallel to the c axis associated with each triangle of Mn dipoles is all that is retained of $P6_3'cm'$. The reduced symmetry leaves Mn dipole moments at arbitrary angles to the crystallographic axes, because Mn ions in sites $6c$ are not constrained by any symmetry.

Scattering amplitudes for the reflection $(0, 0, l)$ with odd l are identical in $P6_3'$ and $P6_3'cm'$, and Eqs. (3) and (4) are valid with reduced symmetry; this is not so for $(h, 0, l)$ and odd l . We demonstrate distinguishing features of reduced symmetry by revisiting $E1-E2$ diffraction and the unrotated amplitude, Eq. (6). At the level of anapoles and quadrupoles,

$$\begin{aligned} (\sigma'\sigma)_{12} &= \text{Eq. (6)} + i(2/5)\sqrt{2} \sin(2\pi hx) \cos(\theta) \sin(\psi) \\ &\times \sin(\beta) [3\langle G_{+1}^1 \rangle' + \sqrt{5}\langle G_{+1}^2 \rangle'' + \dots], \end{aligned} \quad (9)$$

with $\langle G_{\xi}^1 \rangle = -\sqrt{2}\langle G_{+1}^1 \rangle'$, and β is defined in Eq. (5). Dirac multipoles forbidden in the higher symmetry $P6_3'cm'$ have a different dependence on the azimuthal angle and β .

V. DISCUSSION AND CONCLUSIONS

In summary, we have studied a magnetic symmetry ($P6_3'cm'$) that is a well-established description of hex-YMnO₃ [5]. New diffraction data provide motivation to add to the extensive literature on the multiferroic material [14]. Curiously, the diffraction pattern of symmetry $P6_3'cm'$ has not been published. In keeping with previous studies, it allows canting of axial Mn dipoles out of the hexagonal plane [29,30]. Here, patterns for magnetic neutron and resonant x-ray diffraction are derived from the electronic structure factor, Eq. (A1), for Mn ions in sites $6c$, which hosts axial and polar (Dirac) magnetism. We exploit elementary magnetic crystallography, whereby symmetries of occupied sites and the magnetic unit cell are paramount. Encapsulating atomic properties of a material in electronic multipoles with discrete symmetries, in both space and time, enables symmetry informed calculations of diffraction patterns that can be confronted with observations; cf. Table I.

The chiral vector in $P6_3'cm'$ parallel to the c axis associated with each triangle of Mn axial dipoles (Fig. 1) dictates the diffraction pattern for reflection vectors $(0, 0, l)$. Specifically, it fixes angular anisotropy labeled by projections Q of the atomic multipoles $\langle T_Q^K \rangle$ with integer rank K and $-K \leq Q \leq K$ (Table I). The result $Q = 3n$ is self-evident, and scattering amplitudes for x-ray diffraction enhanced by an electric dipole-electric dipole ($E1-E1$; $K = 0, 1, 2$) absorption event use $Q = 0$. In consequence, Bragg spot intensities do not change with rotation of the crystal about the reflection vector (an azimuthal angle scan). We find no intensity in unrotated channels of polarization (Fig. 3) and Eq. (3) for the rotated channel; both findings are consistent with data gathered on hex-YMnO₃ at a temperature of 10 K at the space group forbidden reflection $(0, 0, 1)$ [14]. Moreover, intensities measured at the $L_{2,3}$ absorption edges are equal, to a good approximation [14]. The observation implies that Mn orbital states are negligible in the dipole $\langle T_{\xi}^1 \rangle$ if intensities are enhanced by an $E1-E1$ event, and appropriate sum rules are examined in Appendix B. Dirac multipoles contribute to

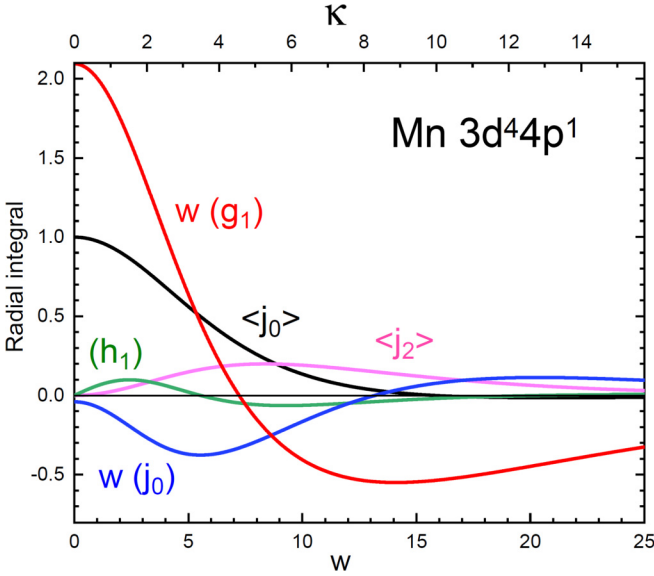


FIG. 4. Radial integrals for $3d^4$ (Mn^{3+}) displayed as a function of the magnitude of the reflection vector $\kappa = 4\pi s$ with $s = \sin(\theta)/\lambda$ (\AA^{-1}), Bragg angle θ , and neutron wavelength λ . Also, a dimensionless variable $w = 3a_o\kappa$ where a_o is the Bohr radius and κ is in units of \AA^{-1} . Black and purple lines are standard radial integrals $\langle j_0(\kappa) \rangle$ and $\langle j_2(\kappa) \rangle$ that occur in the axial dipole, Eq. (C1). Red, green, and blue curves are radial integrals in the polar dipole, Eq. (C2). Two integrals $\langle g_1 \rangle$ and $\langle j_0 \rangle$ diverge in the forward direction of scattering, and quantities $w(g_1)$ and $w(j_0)$ are displayed for this reason. Calculations were performed with Cowan's atomic code [36,37], and figure was made by G. van der Laan.

diffraction enhanced by a parity-odd $E1-E2$ event. As with parity-even $E1-E1$, unrotated amplitudes are zero. Equation (4) for the rotated amplitude is proportional to the diagonal component of the Dirac quadrupole and independent of the azimuthal angle. $E1-E1$ and $E1-E2$ amplitudes differ with respect to phase and the Bragg angle. Nonmagnetic polar multipoles that are signatures of the polar character of the space group have zero amplitudes for $(0, 0, l)$ with odd l . Looking ahead to future experiments, an anapole depicted in Fig. 2 parallel to the tertiary symmetry direction $[1, 2, 0]$ contributes to all $E1-E2$ amplitudes with a reflection vector $(h, 0, l)$ with odd l , e.g., Eq. (6).

Magnetic neutron diffraction by space group $P6_3'cm'$ is discussed in Appendix C using $(h, 0, l)$ with odd l . Unlike x-ray diffraction, multipoles for neutron diffraction depend on the magnitude of the reflection vector. It takes the form of weighted averages of the atomic radial wave function. Figure 4 depicts all radial integrals pertinent to our discussion of diffraction by Mn ions. Two appear in the transition-metal dipole (C1), and the anapole (C2) contains three, two of which diverge in the forward direction. Diffraction by axial multipoles includes a dipole parallel to the ξ axis $[1, 0, 0]$ that is likely the dominant feature at small wave vectors $\kappa \approx 0$; cf. Fig. 4. A quadrupole due to the correlation of the spin anapole ($\mathbf{S} \times \mathbf{n}$) and orbital \mathbf{n} operators enters at around $\kappa \approx 6 \text{\AA}^{-1}$. Notable features of diffraction by Dirac multipoles are contributions by quadrupoles $\langle \mathbf{H}^2 \rangle \propto [(h_1) \langle \{\mathbf{S} \otimes \mathbf{n}\}^2 \rangle]$, with

the radial integral (h_1) depicted in Fig. 4. The exact same quadrupoles explain neutron diffraction from high- T_c compounds Hg1201 and YBCO [23,24].

Resonant x-ray diffraction presented by the magnetic structure $P6_3'$ is discussed in Sec. IV; it is in the history of hex- YMnO_3 [4,5]. Manganese ions occupy sites in $P6_3'$ that have no symmetry. Even so, patterns for $P6_3'$ and $P6_3'cm'$ are identical for reflections $(0, 0, l)$ with odd l . Scope to observe the reduced symmetry in $P6_3'$ exists in reflections $(h, 0, l)$ and odd l . To this end, we give the $E1-E2$ unrotated amplitude Eq. (9).

ACKNOWLEDGMENTS

A discussion with Dr. Y. Joly unmasked the difference between results from a simulation reported in Ref. [14] and the present work [15]. Dr. V. Scagnoli provided Fig. 2. Prof. G. van der Laan performed calculations of atomic radial integrals depicted in Fig. 4. Valuable guidance on the use of crystallography came from Dr. K. S. Knight.

APPENDIX A: ELECTRONIC STRUCTURE FACTOR

The electronic structure factor is defined by Eq. (1). Let $\Phi = \sigma_\theta(-1)^{l+Q}$, with $\Phi = -(-1)^{l+Q}$ for Dirac multipoles, and $\Phi = (-1)^{l+K+Q}$ for $E1-E1$ and $E2-E2$. For a reflection vector (h, k, l) and sites $6c$ in symmetry $P6_3'cm'$,

$$\Psi_Q^K(6c) = \langle O_Q^K \rangle [\alpha + \alpha^* \Phi + \exp(i2\pi Q/3)\{\beta + \beta^* \Phi\} + \exp(-i2\pi Q/3)\Phi\{\alpha\beta + \alpha^* \beta^* \Phi\}]. \quad (\text{A1})$$

Here, $\alpha = \exp(i2\pi hx)$ and $\beta = \exp(i2\pi kx)$, with $x \approx 0.342$ [6]. As the material is ferroelectric (polarization along the c axis), the structure factor is arbitrary to within a phase that we set equal to unity ($z = 0$).

APPENDIX B: SUM RULES

Subsequent results are L edge reduced matrix elements (RMEs) of electronic multipoles $\langle \chi || O^K || \chi' \rangle$, where χ is a composite label for necessary quantum numbers excluding projections Q . An expectation value $\langle O_Q^K \rangle$ is a sum of RMEs each multiplied by a $3j$ symbol that is the sole bearer of Q (Wigner-Eckart theorem). Furthermore, an RME is written in terms of standard unit tensors $W^{(a,b)K}$ with spin variable $a = 0$ or 1 , an orbital variable b , and even $(a + b + K)$ [20]. There are equivalent operators for unit tensors that expose their physical content. Equivalent operators for dipoles are $W^{(1,0)1} \propto \mathbf{S}$, $W^{(0,1)1} \propto \mathbf{L}$, and $W^{(1,2)1} \propto [\mathbf{S}(\mathbf{R} \cdot \mathbf{R}) - 3\mathbf{R}(\mathbf{S} \cdot \mathbf{R})]$ where \mathbf{R} is the position operator conjugate to \mathbf{L} . For the $E1-E1$ dipole $\langle \mathbf{T}^1 \rangle$,

$$A = -\sqrt{(1/30)}W^{(0,1)1}, \\ B = 1/(3\sqrt{15})[W^{(1,0)1} - \sqrt{35}W^{(1,2)1}]. \quad (\text{B1})$$

The coefficients are correct for L edges and d -like valence states. Turning to RMEs for $E2-E2$ and $2p \rightarrow 4p$, A is the same as for $E1-E1$ with $\langle \mathbf{T}^1 \rangle$ an expectation value of Mn $4p$ states. Orbital B is the sum of a dipole and an octupole $W^{(1,2)3}$

that determines $\langle T_0^3 \rangle$ in $(\pi'\sigma)_{22}$. For an $E2-E2$ event,

$$B = -1/(3\sqrt{5})[W^{(1,0)1} - W^{(1,2)1}] - \sqrt{(2/15)}W^{(1,2)3}, \quad (\text{B2})$$

with $\langle T_0^3 \rangle \propto \langle W^{(1,2)3} \rangle_0 \propto \langle [5S_\zeta R_\zeta^2 - 2S_\zeta(\mathbf{R} \cdot \mathbf{R}) - R_\zeta(\mathbf{S} \cdot \mathbf{R})] \rangle$.

RMEs for an $E1-E2$ event are listed by Lovesey and Balcar [31].

APPENDIX C: MAGNETIC NEUTRON DIFFRACTION

Magnetic multipoles in neutron diffraction depend on the magnitude of the reflection vector, κ [22,33,34]. A nominal Mn electronic configuration $3d^4$ (Mn^{3+}) with a high-spin configuration $S = L = 2$ and total angular momentum $J = 0$ is used for RMEs of parity-even neutron multipoles; cf. Table I of Ref. [22].

An axial dipole $\langle \mathbf{T}^1 \rangle$ contains $\langle j_0(\kappa) \rangle$ and $\langle j_2(\kappa) \rangle$, which are averages of spherical Bessel functions of order 0 and 2 with respect to the radial density of the open shell. By definition, $\langle j_0(0) \rangle = 1$ and $\langle j_2(0) \rangle = 0$, and results in Fig. 4 are illustrative of their dependence on κ [34]. A guide to the transition-metal dipole,

$$\langle \mathbf{t}^1 \rangle \approx (\langle \boldsymbol{\mu} \rangle / 3) [\langle j_0(\kappa) \rangle + \langle j_2(\kappa) \rangle (g - 2) / g], \quad (\text{C1})$$

is often used [32,35]. Here, the magnetic moment $\langle \boldsymbol{\mu} \rangle = g\langle \mathbf{S} \rangle$ and the orbital moment $\langle \mathbf{L} \rangle = [(g - 2)\langle \mathbf{S} \rangle]$. The coefficient of $\langle \mathbf{L} \rangle$ in Eq. (C1) is approximate, while $\langle \mathbf{T}^1 \rangle = (1/3)(2\mathbf{S} + \mathbf{L})$ for $\kappa \rightarrow 0$ is an exact result. Multipoles with even K arise from electron spin and spatial degrees of freedom; e.g., $\langle t_0^2 \rangle \propto [\langle j_2(\kappa) \rangle \langle (\mathbf{S} \times \mathbf{n})_0 n_0 \rangle]$ with $\mathbf{n} = \mathbf{R}/R$, and a maximum of $\langle j_2(\kappa) \rangle$ around $\kappa \approx 6 \text{ \AA}^{-1}$ [22]. Axial multipoles have ranks $K = 1 - 5$ for d -type ions. Intensity of a magnetic Bragg spot = $|\langle \mathbf{Q}_\perp \rangle|^2$ when the neutron beam is unpolarized [22,32]. In more detail, $\langle \mathbf{Q}_\perp \rangle^{(\pm)} = [\mathbf{e} \times (\langle \mathbf{Q} \rangle^{(\pm)} \times \mathbf{e})]$ with a unit vector $\mathbf{e} = \kappa/\kappa$, and superscripts refer to axial (+) and Dirac (−) multipoles. The intermediate amplitude $\langle \mathbf{Q} \rangle^{(+)}$ is proportional to the axial magnetic moment $\langle \boldsymbol{\mu} \rangle$ in the forward direction of scattering, with $\langle \mathbf{Q} \rangle^{(+)} = \langle \boldsymbol{\mu} \rangle / 2$ for $\kappa = 0$, while

the dipole in $\langle \mathbf{Q} \rangle^{(-)}$ can be related to anapoles [22,36]. In place of Eq. (C1), the Dirac dipole $\langle \mathbf{d} \rangle$ depends on three radial integrals,

$$\langle \mathbf{d} \rangle = (1/2)[i(g_1)\langle \mathbf{n} \rangle + 3(h_1)\langle \mathbf{S} \times \mathbf{n} \rangle - (j_0)\langle \boldsymbol{\Omega} \rangle]. \quad (\text{C2})$$

Radial integrals (g_1) and (j_0) depicted in Fig. 4 diverge in the forward direction of scattering. Not so for (h_1) that accompanies a spin anapole $\langle \mathbf{S} \times \mathbf{n} \rangle$. It is also the κ dependence of the Dirac quadrupole $\langle \mathbf{H}^2 \rangle \propto [(h_1)\langle (\mathbf{S} \otimes \mathbf{n})^2 \rangle]$ observed in neutron diffraction from high- T_c compounds Hg1201 and YBCO [23,24]. Returning to Eq. (C2), $\langle \boldsymbol{\Omega} \rangle = [(\mathbf{L} \times \mathbf{n}) - (\mathbf{n} \times \mathbf{L})]$ is an orbital anapole (toroidal dipole), depicted in Fig. 2.

Neutron scattering amplitudes for $\kappa = (0, 0, l)$ with odd l are identically zero, for both axial and Dirac multipoles. Results for $(h, 0, l)$ and odd l are complicated and we limit results to low-order multipoles $K = 1, 2, 3$. Amplitudes have a common factor $[2i \sin(2\pi hx)]$ that we omit from the following results. With $\mathbf{e} = (e_\xi, e_\eta, e_\zeta) = (h\sqrt{3}, h, rl\sqrt{3})/Z$ and $\mathbf{e} \cdot \mathbf{e} = 1$,

$$\begin{aligned} \langle Q_\xi \rangle^{(+)} &\approx (9/4)\langle t_\xi^1 \rangle + (3/2)\sqrt{3}e_\zeta^2 \langle t_{+1}^2 \rangle'' \\ &\quad + (3/16)\sqrt{21}(3 - 7e_\zeta^2)\langle t_{+1}^3 \rangle', \\ \langle Q_\eta \rangle^{(+)} &\approx (3/4)\sqrt{3}\langle t_\xi^1 \rangle + (3/2)e_\zeta^2 \langle t_{+1}^2 \rangle'' \\ &\quad + (3/4)\sqrt{7}(7e_\eta^2 - 1)\langle t_{+1}^3 \rangle', \\ \langle Q_\zeta \rangle^{(+)} &\approx -6e_\eta e_\zeta (\langle t_{+1}^2 \rangle'' + \sqrt{7}\langle t_{+1}^3 \rangle'). \end{aligned} \quad (\text{C3})$$

The intensity for $(h, 0, l)$ with odd l ,

$$|\langle \mathbf{Q}_\perp \rangle^{(+)}|^2 \approx (9/4)\sqrt{3}e_\zeta^2 \langle t_\xi^1 \rangle [\sqrt{3}\langle t_\xi^1 \rangle + 16e_\eta^2 \langle t_{+1}^2 \rangle''], \quad (\text{C4})$$

to a good approximation at a level of dipoles and quadrupoles. The equivalent intensity for diffraction by the Mn anapole and Dirac quadrupole $\langle H_{+1}^2 \rangle'$ is

$$|\langle \mathbf{Q}_\perp \rangle^{(-)}|^2 \approx 3(2e_\zeta^2 + 1)[\langle d_\eta \rangle + (3/\sqrt{5})(2e_\zeta^2 - 1)\langle H_{+1}^2 \rangle']^2. \quad (\text{C5})$$

Both intensities vanish for $h = 0$ by virtue of a common factor $[\sin(2\pi hx)]^2$ not shown explicitly.

-
- [1] H. L. Yakel, W. C. Koehler, E. F. Bertaut, and E. F. Forrat, *Acta Crystallogr.* **16**, 957 (1963).
- [2] B. B. Van Aken, T. T. M. Palstra, A. Filippetti, and N. A. Spaldin, *Nat. Mater.* **3**, 164 (2004).
- [3] M. Fiebig, D. Fröhlich, K. Kohn, St. Leute, Th. Lottermoser, V. V. Pavlov, and R. V. Pisarev, *Phys. Rev. Lett.* **84**, 5620 (2000).
- [4] P. J. Brown and T. Chatterji, *J. Phys.: Condens. Matter* **18**, 10085 (2006).
- [5] C. J. Howard, B. J. Campbell, H. T. Stokes, M. A. Carpenter, and R. I. Thomson, *Acta Crystallogr. B* **69**, 534 (2013).
- [6] R. I. Thomson, T. Chatterji, C. J. Howard, T. T. M. Palstra, and M. A. Carpenter, *J. Phys.: Condens. Matter* **26**, 045901 (2014).
- [7] T. N. Tošić, Q. N. Meier, and N. A. Spaldin, *Phys. Rev. Res.* **4**, 033204 (2022).
- [8] B. Gilbert, B. H. Frazer, A. Belz, P. G. Conrad, K. H. Neelson, D. Haskel, J. C. Lang, G. Srajer, and G. De Stasio, *J. Phys. Chem. A* **107**, 2839 (2003).
- [9] J. Herrero-Martín, J. García, G. Subías, J. Blasco, and M. C. Sánchez, *Phys. Rev. B* **70**, 024408 (2004).
- [10] J. Herrero-Martín, J. García, J. Blasco, and G. Subías, *Eur. Phys. J.: Spec. Top.* **208**, 107 (2012).
- [11] J. Voigt, J. Persson, J. W. Kim, G. Bihlmayer, and Th. Brückel, *Phys. Rev. B* **76**, 104431 (2007).
- [12] D. Mannix, D. F. McMorro, R. A. Ewings, A. T. Boothroyd, D. Prabhakaran, Y. Joly, B. Janousova, C. Mazzoli, L. Paolasini, and S. B. Wilkins, *Phys. Rev. B* **76**, 184420 (2007).
- [13] L. Paolasini, *Collect. SFN* **13**, 03002 (2014).
- [14] M. Ramakrishnan, Y. Joly, Q. N. Meier, M. Fechner, M. Porer, S. Parchenko, Y. W. Windsor, E. M. Bothschafter, F. Lichtenberg, and U. Staub, *Phys. Rev. Res.* **5**, 013203 (2023).
- [15] Y. Joly (private communication, 2023); *ab initio* simulations using FDMNES in Ref. [14] have been withdrawn.

- [16] We use the Belov-Neronova-Smirnova (BNS) setting of magnetic space groups: see Bilbao Crystallographic server, <http://www.cryst.ehu.es>.
- [17] MAGNDATA, <http://webbdcristal.ehu.es/magndata>.
- [18] S. W. Lovesey and V. Scagnoli, *J. Phys.: Condens. Matter* **21**, 474214 (2009).
- [19] J. Luo, G. T. Trammell, and J. P. Hannon, *Phys. Rev. Lett.* **71**, 287 (1993).
- [20] S. W. Lovesey, E. Balcar, K. S. Knight, and J. Fernández Rodríguez, *Phys. Rep.* **411**, 233 (2005).
- [21] V. Scagnoli, U. Staub, Y. Bodenthin, R. A. De Souza, M. García-Fernández, M. Garganourakis, A. T. Boothroyd, D. Prabhakaran, and S. W. Lovesey, *Science* **332**, 696 (2011).
- [22] S. W. Lovesey, *Phys. Scr.* **90**, 108011 (2015).
- [23] S. W. Lovesey, D. D. Khalyavin, and U. Staub, *J. Phys.: Condens. Matter* **27**, 292201 (2015).
- [24] S. W. Lovesey and D. D. Khalyavin, *J. Phys.: Condens. Matter* **27**, 495601 (2015).
- [25] G. van der Laan and A. I. Figueroa, *International Tables of Crystallography* (Springer, Berlin, 2022), Vol. I.
- [26] V. Scagnoli and S. W. Lovesey, *Phys. Rev. B* **79**, 035111 (2009).
- [27] B. T. Thole, P. Carra, F. Sette, and G. van der Laan, *Phys. Rev. Lett.* **68**, 1943 (1992); P. Carra, B. T. Thole, M. Altarelli, and X. D. Wang, *ibid.* **70**, 694 (1993); P. Carra, H. König, B. T. Thole, and M. Altarelli, *Phys. B (Amsterdam)* **192**, 182 (1993).
- [28] S. W. Lovesey, *J. Phys.: Condens. Matter* **10**, 2505 (1998).
- [29] C. Degenhardt, M. Fiebig, D. Fröhlich, Th. Lottermoser, and R. V. Pisarev, *Appl. Phys. B* **73**, 139 (2001).
- [30] I. V. Solovyev, M. V. Valentyuk, and V. V. Mazurenko, *Phys. Rev. B* **86**, 054407 (2012).
- [31] S. W. Lovesey and E. Balcar, *J. Phys. Soc. Jpn.* **79**, 104702 (2010).
- [32] S. W. Lovesey, *Theory of Neutron Scattering from Condensed Matter*, Vol. 2 (Clarendon Press, Oxford, 1987).
- [33] A. T. Boothroyd, *Principles of Neutron Scattering from Condensed Matter* (Oxford University Press, Oxford, UK, 2020).
- [34] P. J. Brown, *International Tables of Crystallography* (Springer, Berlin, 2004), Vol. C.
- [35] G. T. Trammell, *Phys. Rev.* **92**, 1387 (1953).
- [36] G. van der Laan and S. W. Lovesey, *Phys. Rev. B* **103**, 125124 (2021).
- [37] R. D. Cowan, *J. Opt. Soc. Am.*, **58**, 808 (1968); *The Theory of Atomic Structure and Spectra* (University of California Press, Berkeley, CA, 1981).